Electronic Supplementary Information

Metal ion and organic ligand disubstituted bimetallic metal–organic framework nanosheets for high-performance alkaline zinc-based batteries

Huayu Wang, Jie Bai, Qingqing He, Yanxin Liao, and Lingyun Chen *

Department of Applied Chemistry, School of Chemistry and Chemical Engineering,

Chongqing University, Chongqing 401331, China

* E-mail: lychen@cqu.edu.cn

Contents

1. Experimental section

1.1. Preparation of Co_xNi_y-MOF

All reagents and solvents were used directly without further treatments. Co_xNi_y-MOF (x/y = 1:0, 3:1, 1:1, 1:3, and 0:1) was obtained by the metal ion-substitutions strategy. First, 474 mg (2 mmol) of $NiCl_2 \cdot 6H_2O$ were dissolved in 70 mL of deionized water (H_2O) containing 1.0 g poly(vinyl pyrrolidone) (PVP). 166 mg (1.0 mmol) 1, 4-benzenedicarboxylic acid (H_2BDC) was dissolved in 70 mL sodium hydroxide aqueous solution (0.5 mol/L NaOH) and then added to the salt solution. The mixed solution was stirred for 48 hours at ambient conditions and then washed with H_2O three times before drying at 80 °C for 12 h. The synthesis process of Co_xNi_y-MOF is consistent with the process described above, except for the difference in metal ions. Maintain a constant total feed molar amount of metal ions at 2 mmol ($x + y = 2$ mmol), Co_xNi_y-MOF materials with different ratios of x and y (x/y = 1:0, 3:1, 1:1, 1:3, and 0:1) were obtained by introducing Co ions to replace Ni ions, and these MOFs were denoted as Co-MOF, Co_3Ni_1-MOF, Co_1Ni_1-MOF, Co_1Ni_3-MOF, Ni-MOF, respectively.

1.2. Preparation of BS-MOF-*z*

BS-MOF-*z* (z = 5, 10, and 15) was obtained by a ligand modulation strategy. The synthesis of BS-MOF-*z* is similar to Co_xNi_y-MOF, except for the addition of 1,4-Benzenedimethanethiol (BDMT). In detail, 357 mg (1.5 mmol) of $CoCl_2 \cdot 6H_2O$ and 117 mg (0.5 mmol) $NiCl_2 \cdot 6H_2O$ were dissolved in 70 mL of deionized water containing 1.0 g PVP. 166 mg H_2BDC (1.0 mmol) was dissolved in 70 mL sodium hydroxide aqueous solution (0.5 mol/L NaOH) and then added to the salt solution. Subsequently, 1 mL ethanol solution that contains 10 mg 1,4-benzenedimethanethiol (BDMT) was added to the above solution and stirred for 48 h at

ambient conditions. After the reaction was completed, the obtained product (labeled as BS-MOF-10) was rinsed with H_2O three times and dried at 80 °C for 12 h. Other BS-MOF samples prepared with different BDMT masses (5 mg and 15 mg) were synthesized using the same method and named BS-MOF-5 and BS-MOF-15, respectively.

1.3. Materials characterizations

The morphology of the prepared samples was investigated by scanning electron microscope (SEM, HITACHI S-4800 electron microscopy) and transmission electron microscope (TEM, Tecnai G2 F20 S-Twin). The crystal structure of the materials was analyzed by X-ray diffraction spectroscopy (XRD) on a Bruker D8 Advanced Powder X-ray Diffractometer (Cu Kα radiation: $\lambda = 0.15406$ nm). The nitrogen (N_2) adsorption–desorption isotherms and pore size of the samples were performed on Brunauer Emmett–Teller (BET) surface analyzer (Micromeritics, ASAP 2020). The chemical environment of the obtained products was studied using X-ray photoelectron spectroscopy (XPS, ESCALAB 250Xi, ThermoFisher Scientific). Fourier Transform Infrared Spectroscopy (FTIR) was measured on Nicolet iS50. The Raman spectrum was texted using a wavelength of 633 nm as the laser source (LabRAM HR Evolution). The thermogravimetric analysis (TGA) measurements (SDTQ600)) were performed in N_2 atmosphere to study the thermal stability of materials. Inductively coupled plasma optical emission spectrometer (ICP-OES, iCAP 6300 Duo) was used to analyze the composition of the sample.

1.4. Electrochemical measurements

Cyclic voltammetry (CV) and electrochemical impedance spectroscopy (EIS, frequency range: 0.01 Hz to 100 kHz) were measured using an electrochemical working station

(CHI760E, Chenhua). Galvanostatic charge-discharge (GCD) and cycling stability tests were performed based on the LAND battery testing system (CT3001A). The cathode was prepared by coating MOFs on nickel foam (NF). The NF (1 cm × 3 cm) was first ultrasonically with acetone, 2 M HCl, absolute ethanol and distilled water alternately for 15 minutes to remove impurities on the surface, and then overnight dried in a vacuum oven at 80 ℃. The samples, polyvinylidene fluoride and acetylene black were mixed at a wt% of 7:1:2 with N-methyl 2-pyrrolidone as the solvent and ultrasonic for half an hour to form a homogeneous slurry, coated on the pre-treated NF (coating area is 1 cm × 1cm). The mass loading of the active materials was about 0.9~1.5 mg cm^{-2} after drying at 100 °C for 12 h in a vacuum oven. A two-electrode system was used to evaluate the electrochemical performance of the alkaline Zn-based battery in 2 M KOH and 0.2 M $Zn(CH_3COO)_2$ ($Zn(AC)_2$) solution, where the obtained material and Zn plate were studied as cathode and anode, respectively.

2. Supplementary Methods

Calculation of Capacitive Contribution:

The peak current (i_p) and scan rate (v) obey the following linear relationship:[1, 2]

$$i_p = av^b \quad (1)$$

$$\log(i_p) = b\log v + \log a \quad (2)$$

The b value is a slope that is calculated from Formula 2 and can reveal whether the electrochemical reaction is controlled by a surface-capacitive controlled process or a diffusion-controlled process. When b=1, it represents that the charge storage process is controlled by the redox reaction on the surface (capacitive contribution), while b is 0.5 indicates that the charge storage is controlled by ionic diffusion.

Besides, the ratio of capacitive contribution can be quantified through the following equation:[3, 4]

$$i = k_1 v + k_2 v^{1/2} \quad (3)$$

where $k_1 v$ represents capacitive contribution and $k_2 v^{1/2}$ represents diffusion contribution. At different scan rates, the potential is fixed and k_1 and k_2 remain constant, so the CV curves for different scan rates can be used to calculate k_1 and k_2 at different voltages. The area obtained by connecting the capacitance contributions at individual voltage points is the capacitive contribution at a certain scan rate, and the ratio of its area to the area of the CV diagram is the ratio of the capacitive contribution.

3 Supporting Figures and Tables

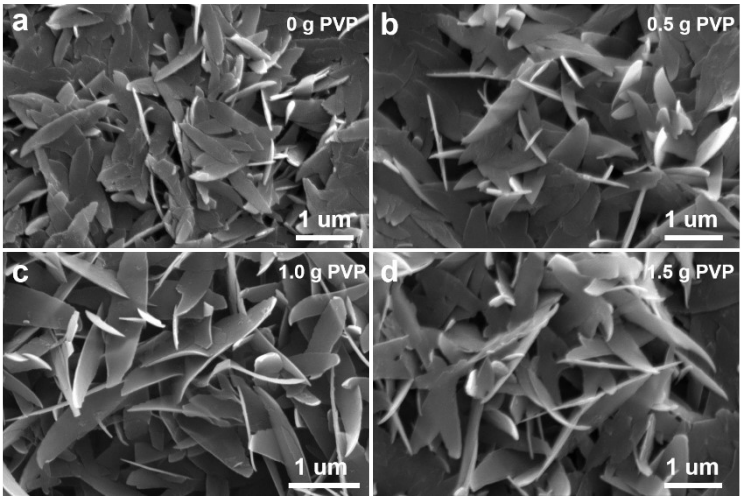

Fig. S1 SEM images of the synthesized Co_3Ni_1-MOF at different PVP concentrations: (a) 0 g PVP, (b) 0.5 g PVP, (a) 1.0 g PVP, and (a) 1.5 g PVP.

The morphology and structure of Co_xNi_y-MOF (x/y = 1:0, 3:1, 1:1, 1:3, and 0:1) precursors were characterized usingSEM. Firstly, Fig. S1 shows the SEM images of the synthesized samples at different PVP concentrations of Co_3Ni_1-MOF, all exhibiting leaf-like nanosheet morphology. The difference is that the agglomerated nanosheets were dispersed with the presence of PVP, and the leaf-like nanosheets gradually crosslink with each other to form an open network structure as the PVP concentration increases, which exhibits more outstanding morphology at the PVP addition of 1.0 g. This result indicates that PVP plays a crucial role in stabilizing the structure.

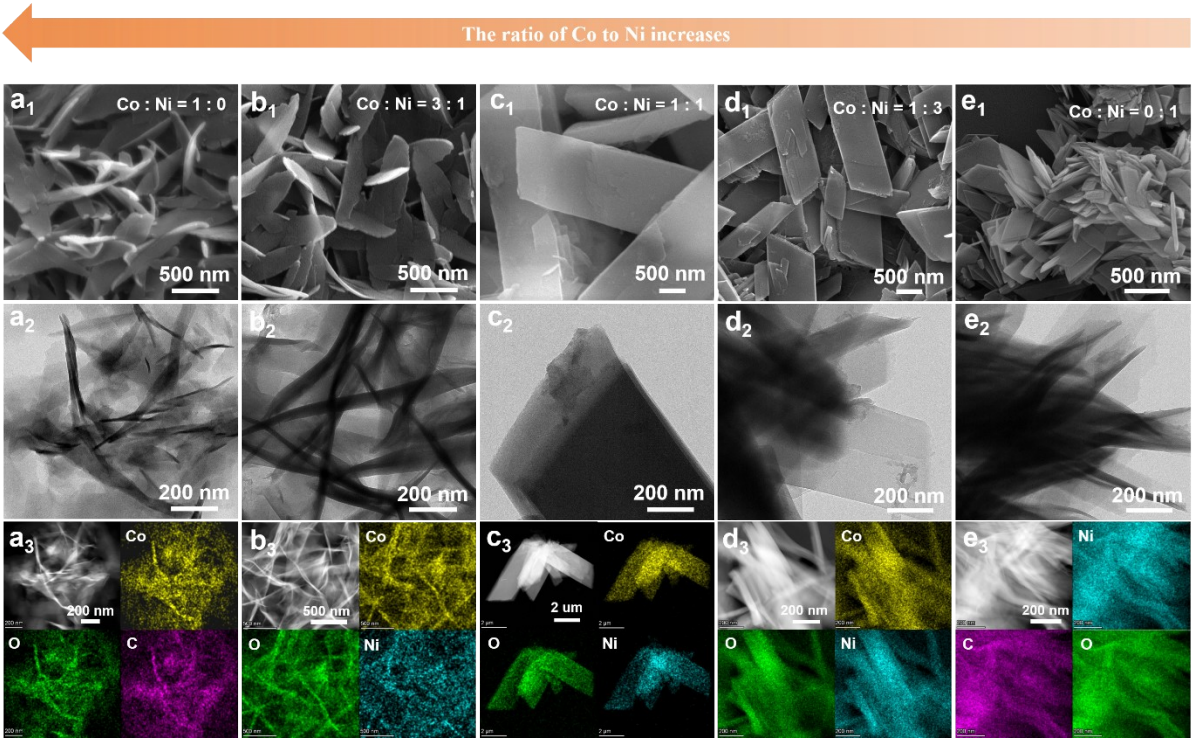

Fig. S2 SEM images, TEM images, and corresponding EDS images of (a_1-a_3) Co-MOF, (b_1-b_3) Co_3Ni_1-MOF, (c_1-c_3) Co_1Ni_1-MOF, (d_1-d_3) Co_1Ni_3-MOF, and (e_1-e_3) Ni-MOF.

In the process of regulating the content of Co and Ni metal ions, the morphology of MOFs remained as the bulk-sheet structure (Ni-MOF) when Ni was replaced by a small portion of Co source (Co_1Ni_3-MOF). With the increase of Co content (no less than Ni source), the morphology and size of MOFs undergo significant changes and exhibit the leaf-like nanosheet structure. The introduction of the Co source has significantly changed the microstructure and macroscopic appearance of MOFs, and the corresponding SEM and transmission electron microscope (TEM) images in Fig. S2 clearly illustrate this process of transformation.

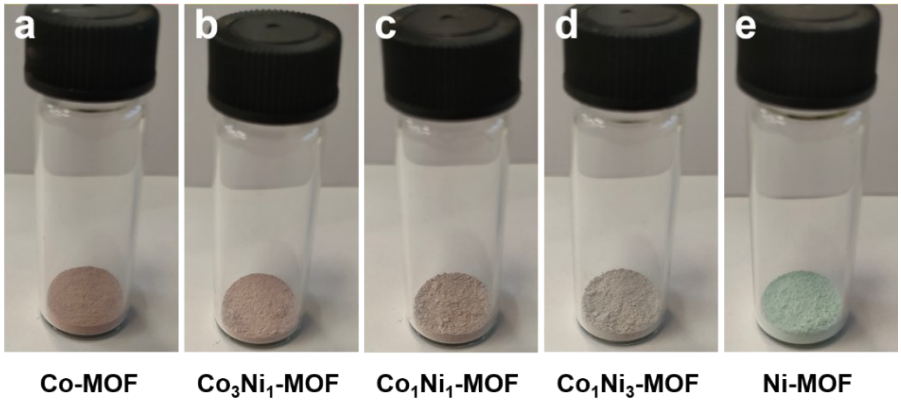

Fig. S3 Digital photos of Co_xNi_y-MOF samples (*x*/*y* = 1:0, 3:1, 1:1, 1:3, and 0:1).

Corresponding digital photos of Co_xNi_y-MOF samples are shown in Fig. S3. Based on the above research, the optimized conditions are that the PVP content is 1.0 g and the molar ratio of Co and Ni is 3: 1.

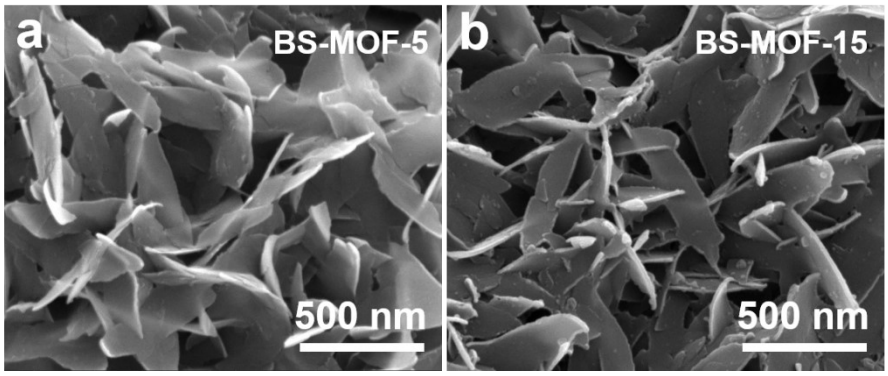

Fig. S4 SEM images of (a) BS-MOF-5 and (b) BS-MOF-15.

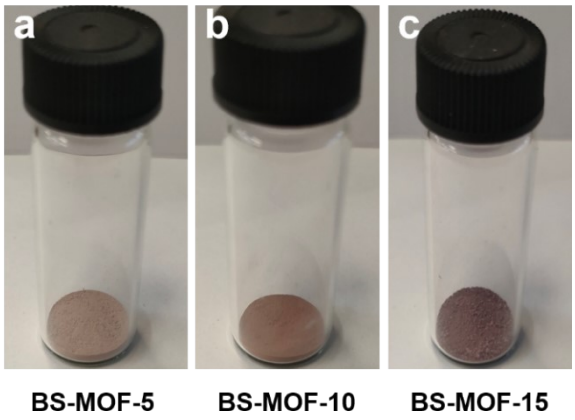

Fig. S5 Digital photos of BS-MOF-*z* samples (*z* = 5, 10, and 15).

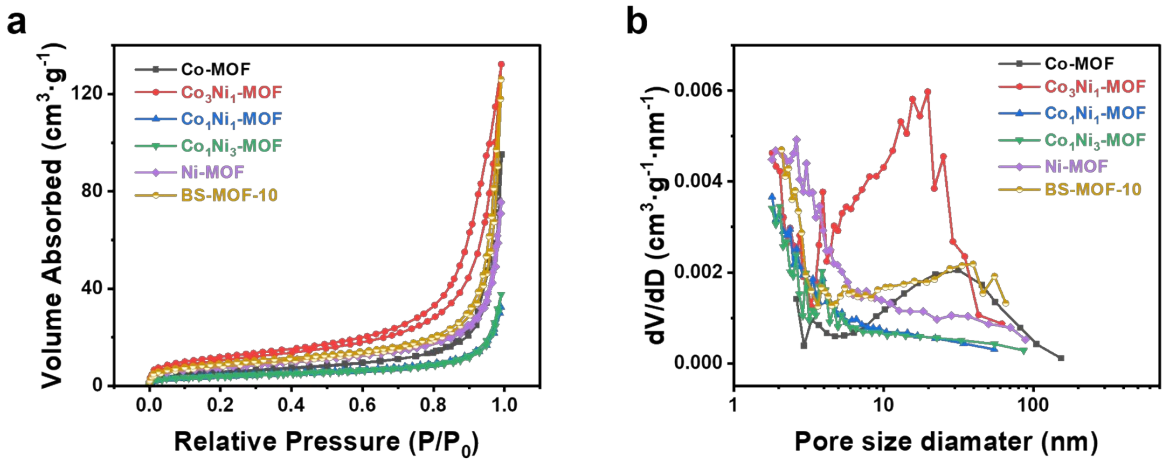

Fig. S6 (a) N_2 adsorption-desorption isotherms and (b) Barret–Joyner–Halenda (BJH) pore size distributions of these prepared MOFs.

Table S1 Specific surface area and pore size of these prepared MOFs.

Sample	BET Surface area (m^2 g^{-1})	Pore volume (cm^3 g^{-1})	Pore size (nm)
Co-MOF	22	0.14	26
Co_3Ni_1-MOF	38	0.20	15
Co_1Ni_1-MOF	14	0.05	11
Co_1Ni_3-MOF	13	0.06	14
Ni-MOF	27	0.11	14
BS-MOF-10	30	0.19	21

The specific surface areas and the pore size of these prepared MOFs were evaluated by Brunauer Emmett-Teller (BET) measurement (Fig. S6). Additional BET-related data on these prepared MOFs are shown in Table S1. The adsorption hysteresis loops are observed in the middle section of the N_2 adsorption-desorption isotherms (Fig. S6a), which can be classified as type IV curves with obvious H3 hysteresis loops according to the latest IUPAC classification. Furthermore, it can be seen from the pore size distribution diagram that the pore size of these materials is mainly distributed between 2-50 nm, and only a few pores are greater than 50 or even 100 nm (Fig. S6b), which can be classified as mesoporous materials.

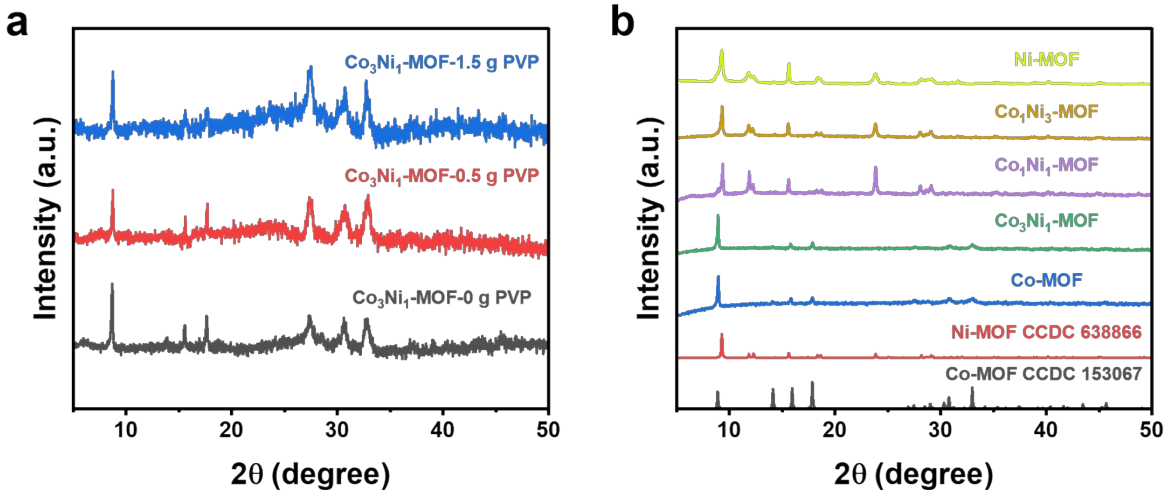

Fig. S7 (a) XRD patterns of the Co_1Ni_3-MOF at different PVP concentrations. (b) XRD patterns of the Co_xNi_y-MOF.

The addition of PVP only affects the morphological regularity of Co_3Ni_1-MOF to a certain extent and has no alteration in the crystal structure (Fig. S7a). The XRD patterns of Co_xNi_y-MOF with different molar ratios of Co/Ni are shown in Fig. S7b. The characteristic peak of the XRD pattern for Co-MOF (x/y = 1:0) can be identified as Co-BDC (Cambridge Crystallographic Data Centre (CCDC) 153067) and the main peak of 2θ at 8.9° corresponds to the (2 0 0) crystal plane of Co-BDC. The XRD pattern of Ni-MOF (x/y = 0:1) is indexed to the diffraction signals of the Ni-BDC phase (CCDC 638866) and the main peak of 2θ at 9.3° corresponds to the (1 0 0) crystal plane of Ni-BDC. As the degree of substitution of Ni by Co increases, the crystal structure of the obtained samples gradually converts from the Ni-BDC phase to the Co-BDC phase. When the molar amount of Co is not lower than Ni, the Ni-BDC phase disappears and only the diffraction peak of Co-BDC exists. The pattern presented by XRD results is consistent with the SEM images.

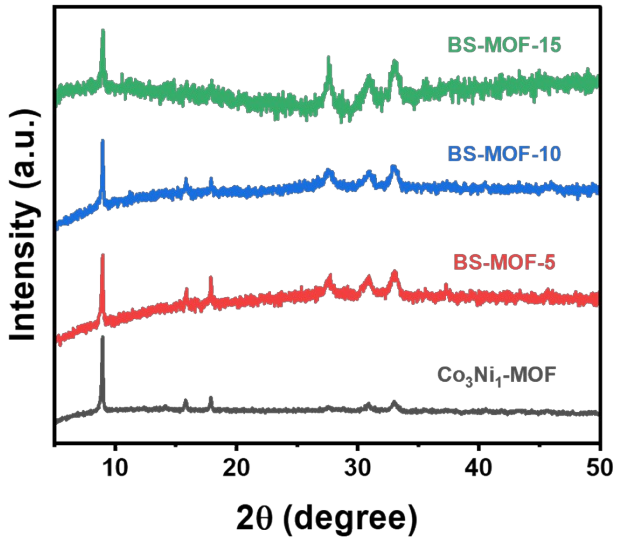

Fig. S8 XRD patterns of BS-MOF.

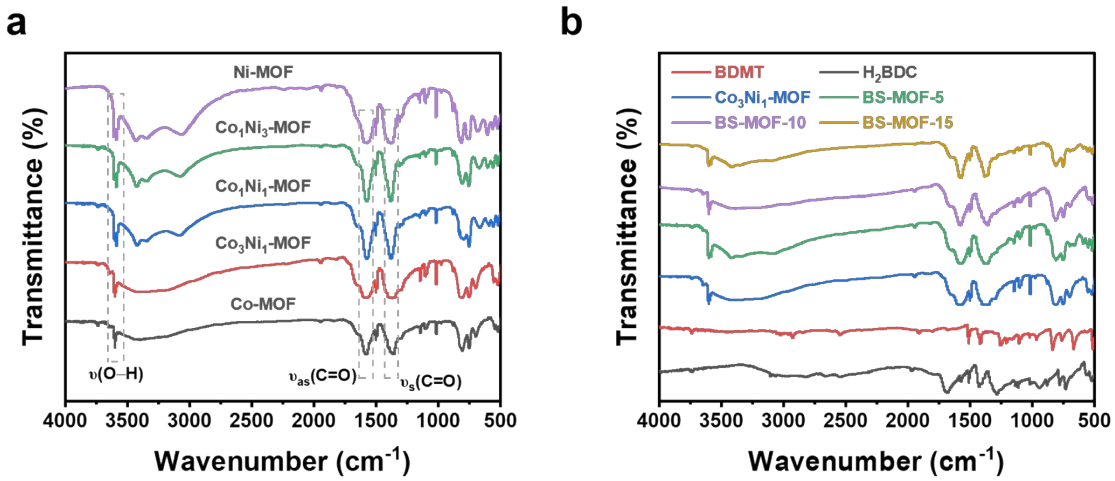

Fig. S9 FTIR spectrums of the (a) Co_xNi_y-MOF and (b) BS-MOF-*z*.

For Co_3Ni_1-MOF, the band at ~3600 cm^{-1} is due to the stretching vibrations of OH^-.[5] The strong bands at 1366 and 1582 cm^{-1} are attributed to the symmetric and asymmetric modes of the coordinated carboxylate groups, respectively.[6] The spectra for Co_xNi_y-MOF samples show almost identical peak positions (Fig. S9a). The FTIR spectrum of the BS-MOF-*z* sample shows a similar shape to Co_3Ni_1-MOF, and no characteristic peak of BDMT was observed, indicating the successful introduction of BDMT ligands (Fig. S9b).

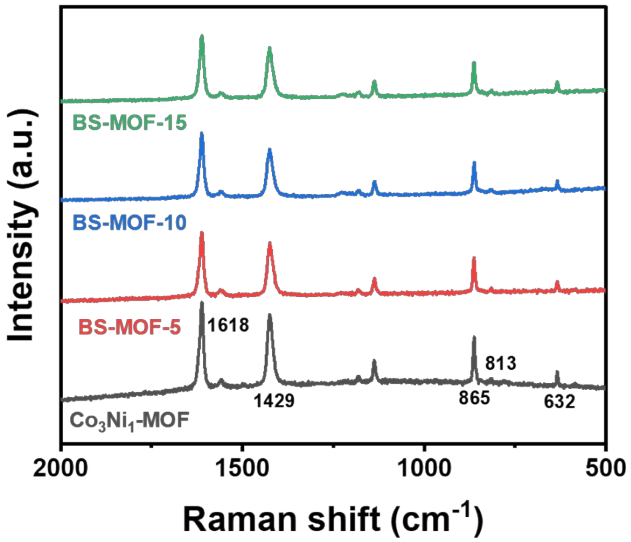

Fig. S10 Raman spectrums of the BS-MOF-*z*.

Raman spectra of Co_3Ni_1-MOF and BS-MOF-*z* share similar bands. The bands at 1618 and 1429 cm^{-1} are attributed to the in- and out-of-phase stretching modes of the coordinated carboxylate groups bond with metal centers.[7] The C-H stretching region of the benzene ring is set at 865, 813, and 632 cm^{-1}.[8]

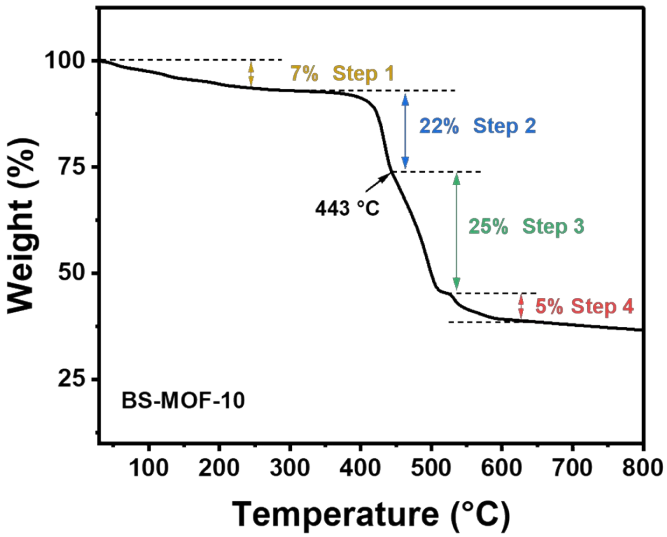

Fig. S11 TGA curves of the as-synthesized BS-MOF-10 in N_2 atmosphere.

The weight loss occurring before 200 ℃ (Step 1) is mainly related to the loss of water molecules adsorbed on the MOF surface, followed by weight loss (Step 2) corresponding to the loss of crystalline water and coordination water in the MOFs. The decomposition of the organic framework in BS-MOF-10 slowly decomposed at 443 ℃, resulting in a total weight loss of 30% (Step 3 and Step 4) within the range of 431-630 ℃.[9, 10]

Table S2 The ICP-OES data of the BS-MOF-10.

Element	Mass content (W, %)	Molar ratio
Co	28.68	1
Ni	7.14	0.25
S	1.41	0.09

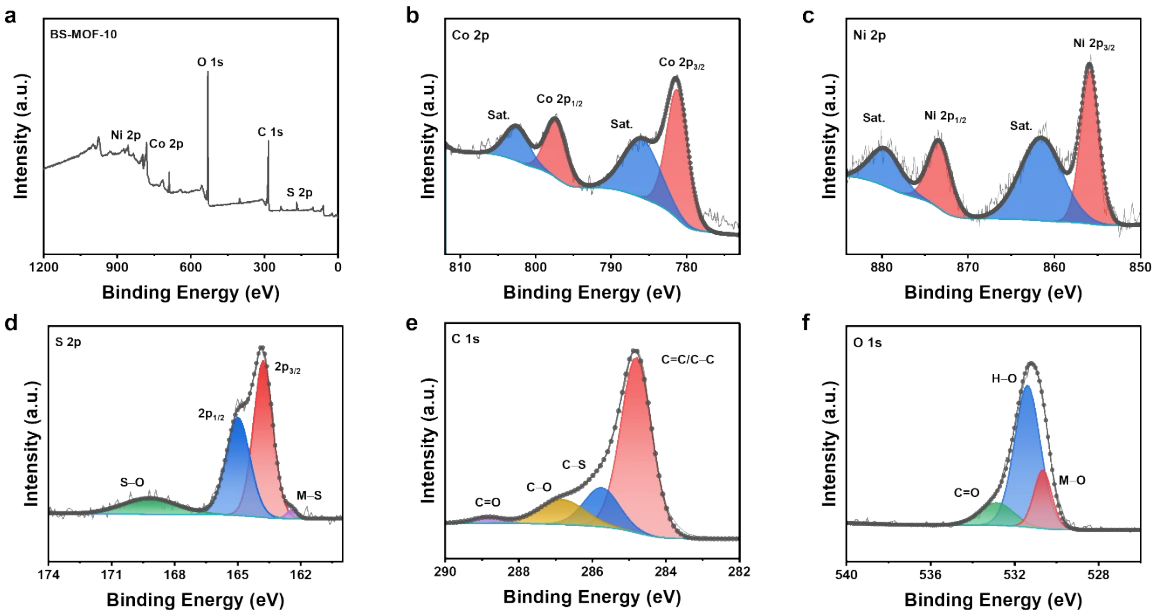

Fig. S12 (a) Full XPS spectra, (b) Co 2p, and (c) Ni 2p, (d) S 2p, (e) C 1s, and (f) O 1s of BS-MOF-10.

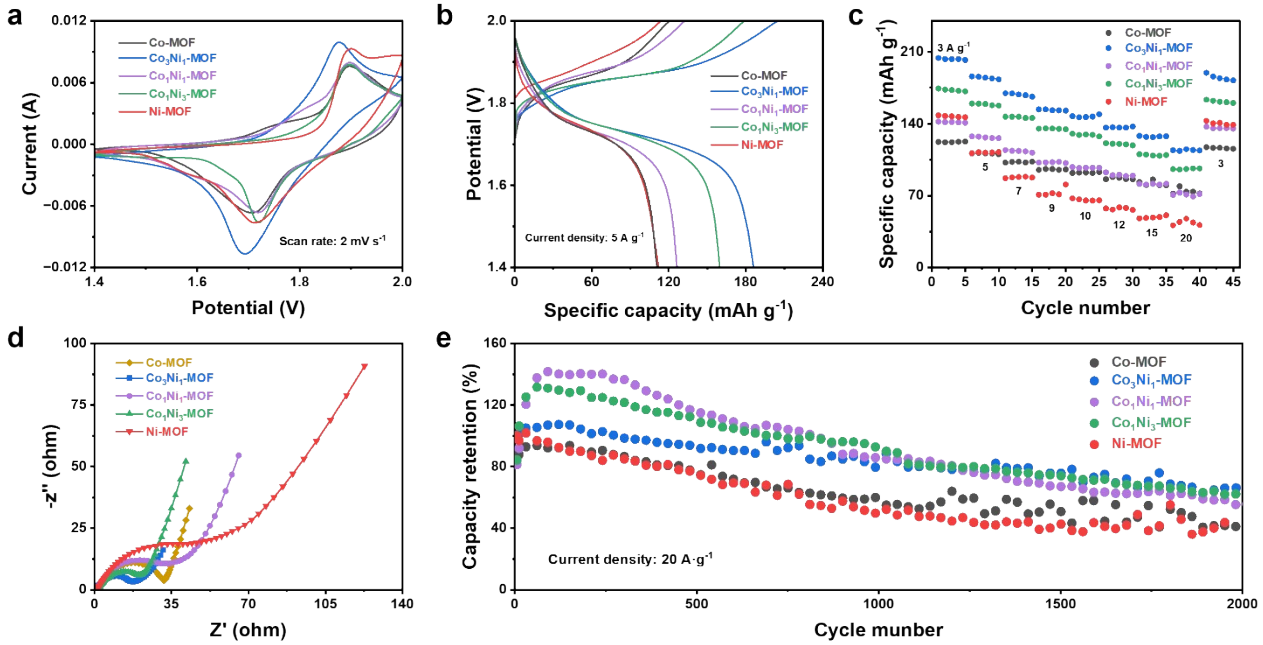

Fig. S13 (a) CV curves at a scan rate of 2 mV s^{-1}, (b) GCD curves at 5 A g^{-1}, (c) Rate performance and corresponding coulombic efficiency at various current densities, (d) Nyquist plots, and (e) Cycling performance at 20 A g^{-1} of Co_xNi_y-MOFs//Zn batteries.

Table S3 The fitted results of EIS data of Co_xNi_y-MOFs.

Sample	R_{ct} (Ω)	R_s (Ω)
Co-MOF	34.1	0.98
Co_3Ni_1-MOF	18.9	0.89
Co_1Ni_1-MOF	41.6	0.92
Co_1Ni_3-MOF	25.6	1.17
Ni-MOF	62.3	1.29

Table S4 The fitted results of EIS data of BS-MOF-*z*.

Sample	R_{ct} (Ω)	R_s (Ω)
BS-MOF-5	18.6	0.86
BS-MOF-10	18.2	0.80
BS-MOF-15	21	0.79

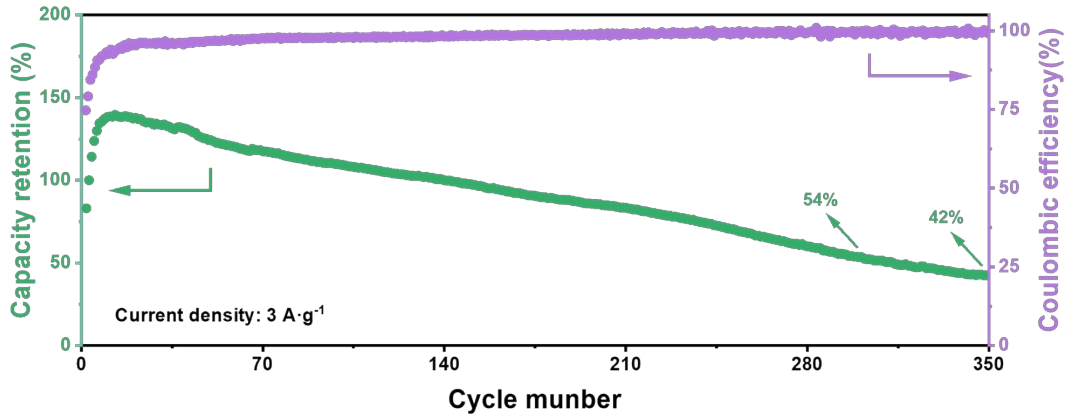

Fig. S14 Cycling performance at 3 A g^{-1} of the BS-MOF-10//Zn battery.

Table S5 The commparison of the electrochemical performance of the Co/Ni-based cathodes for recently reported AZBs.

Cathode	Electrolyte	Mass loading (mg cm^{-2})	Specific capacity	Cycling stability	Ref.
ZNC/NF	6 M KOH + 0.2 M $Zn(AC)_2$	9.2	2.1 mA h cm^{-2} at 5.0 mA cm^{-2}	56% (5000 cycles, 50 mA cm^{-2})	11
NiCo-S-2/RGO	6 M KOH + 0.5 M $Zn(AC)_2$	/	197 mA h g^{-1} at 1.0 A g^{-1}	84% (1000 cycles, 7 A g^{-1})	12
NZMCO	3 M KOH + 0.02 M $Zn(AC)_2$	9.6	1.93 mA h cm^{-2} at 5.0 mA cm^{-2}	85% (30000 cycles, 150 mA cm^{-2})	13
Ni-substitution Co_3O_4	6 M KOH + 0.2 M $Zn(AC)_2$	2.2	272 mA h g^{-1} at 0.25 A g^{-1}	63.9% (2000 cycles, 2 A g^{-1})	14
Co-Ni/NiO@C	6 M KOH + 0.5 mM $Zn(AC)_2$	2.0	321 mA h g^{-1} at 0.625 A g^{-1}	94% (2500 cycles, 12.5 A g^{-1})	15
NNA@CNH-1	1 M KOH	1.0	247 mA h g^{-1} at 1.1 A g^{-1}	88% (5000 cycles, 30 A g^{-1})	16
CNT-V-NiCoSe-400	3 M KOH with saturated ZnO	1.0~2.0	361 mA h g^{-1} at 1.0 A g^{-1}	87% (5000 cycles, 10 A g^{-1})	17
$NiMoO_4$/NF	6 M KOH + 0.2 M $Zn(AC)_2$	/	0.83 mA h cm^{-2} at 1.0 mA cm^{-2}	89% (300 cycles, 10 mA cm^{-2})	18
Ni-Co_9S_8-0.6	2 M KOH + 0.2 M $Zn(AC)_2$		152 mA h g^{-1} at 1.0 A g^{-1}	69% (3000 cycles, 4 A g^{-1})	19
Ni_3S_2@PANI	6 M KOH + 0.2 M $Zn(AC)_2$	/	243 mA h g^{-1} at 5.1 A g^{-1}	100% (5000 cycles, 5.7 A g^{-1})	20
BS-MOF-10	2 M KOH + 0.2 M $Zn(AC)_2$	1.2	361 mA h g^{-1} at 3 A g^{-1}	84% (4000 cycles, 20 A g^{-1})	**This work**

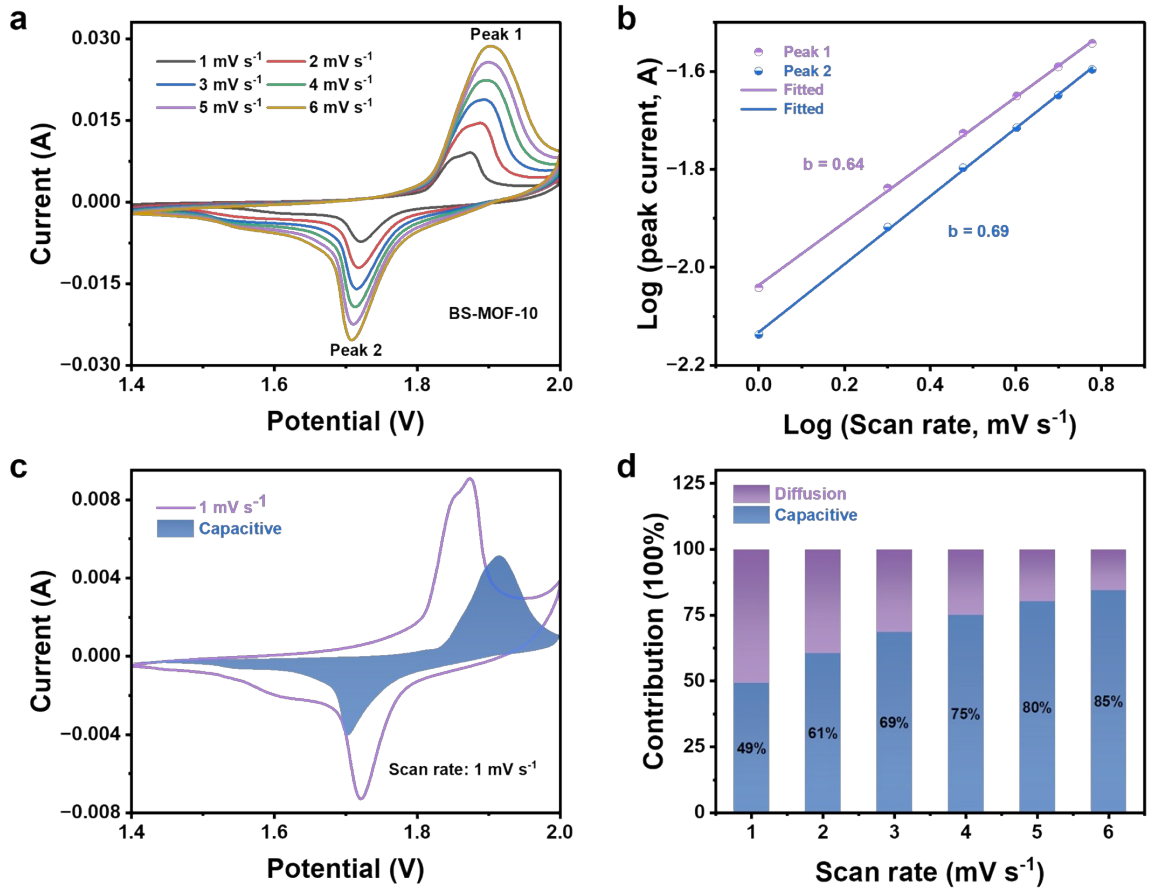

Fig. S15 (a) CV curves, (b) the relationship between log(i_p) and log(v), (c) the capacitive and diffusion-controlled capacities at 1 mV s^{-1}, and (d) contribution ratio of the capacitive and diffusion-controlled capacities at different scan rates of the BS-MOF-10//Zn battery.

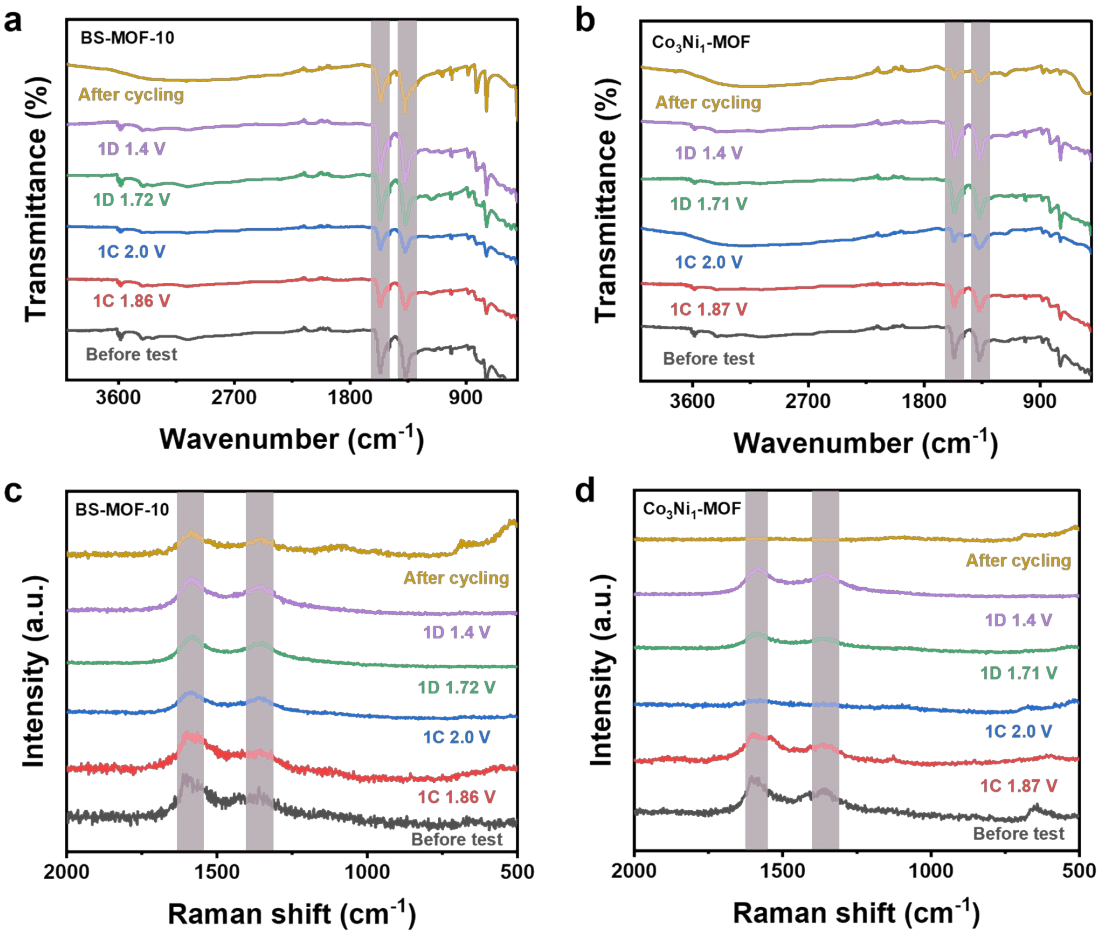

Fig. S16 *Ex situ* FTIR of (a) BS-MOF-10 electrode and (b) Co_3Ni_1-MOF electrode during the first charge–discharge process and after cycling. *Ex situ* Raman spectra of (c) BS-MOF-10 electrode and (d) Co_3Ni_1-MOF electrode during the first charge–discharge process and after cycling.

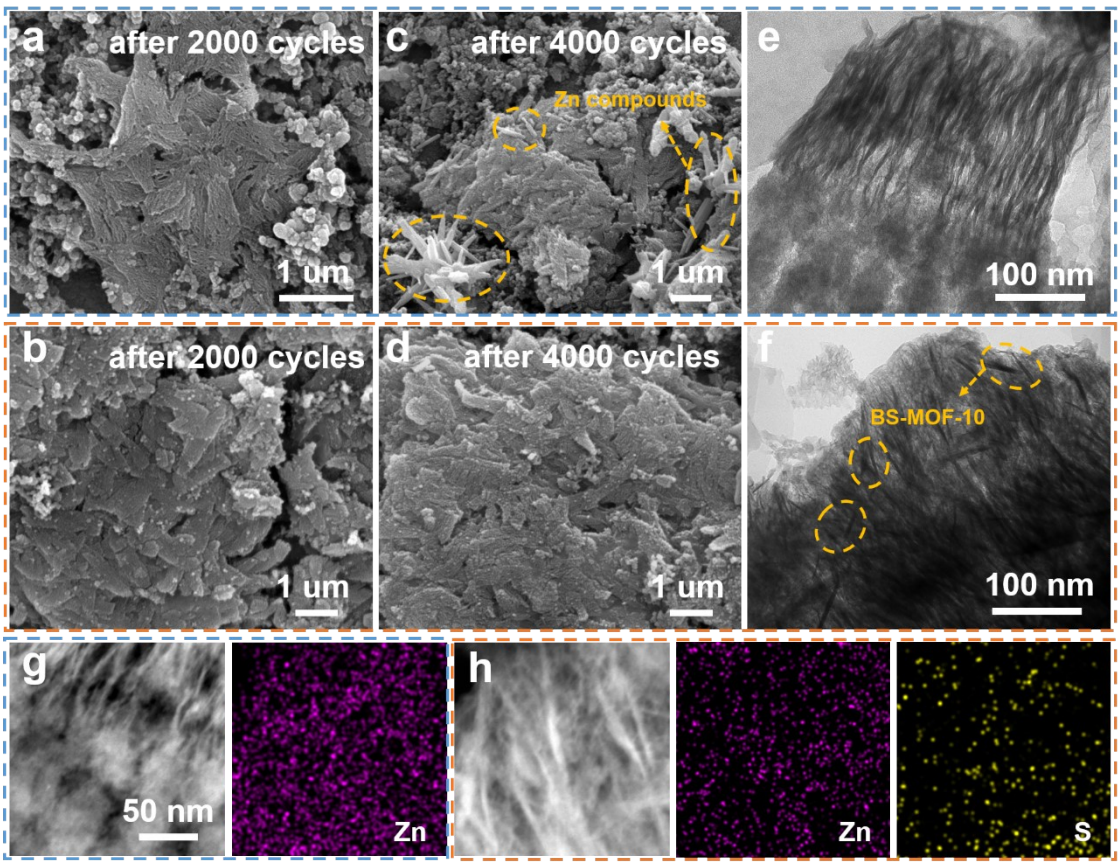

Fig. S17 (a) and (c) *Ex situ* SEM images at different magnifications of Co_3Ni_1-MOF electrode after cycling. (b) and (d) *Ex situ* SEM images at different magnifications of BS-MOF-10 electrode after cycling. *Ex situ* TEM images of (e) Co_3Ni_1-MOF electrode and (f) BS-MOF-10 electrode after 4000 cycles. *Ex situ* EDS images of (g) Co_3Ni_1-MOF electrode and (h) BS-MOF-10 electrode after 4000 cycles.

Ex situ SEM and TEM tests further confirmed the structural stability enhanced by BS-MOF-10. After 2000 cycles, both Co_3Ni_1-MOF (Fig. S17a) and BS-MOF-10 (Fig. S17b) maintained the leaf-like nanosheet structure without significant alterations, exhibiting only slight roughness on the surface of the material. Following 4000 cycles, the structure of Co_3Ni_1-MOF underwent severe collapse (Fig. S17c), and corresponding dendritic-like compounds rich in Zn element were generated (as shown in the yellow area in Fig. S17c), which is also one of the important reasons for the capacity decay in the cyclic testing of Co_3Ni_1-MOF. In

comparison, BS-MOF-10 maintained a well-preserved structure (Fig. S17d), albeit showing slight nanosheet agglomeration and surface decomposition. From *ex situ* TEM images after long cycling (Fig. S17e), it can also be seen that Co_3Ni_1-MOF undergoes dramatic decomposition. Under the same conditions, no morphological change was observed in BS-MOF-10 while a leaf-like nanosheet structure with mutual cross-linking was detected, as depicted in the yellow area in Fig. S17f. The distribution diagram of Zn elements after cycling can further illustrate the structural stability of the material. After cycling, the content of Zn in Co_3Ni_1-MOF (Fig. S17g) is higher than that in BS-MOF-10 (Fig. S17h), that is to say, more Zn is retained in Co_3Ni_1-MOF framework. With the continuous accumulation of Zn content during the cycling process, Zn-rich compounds, also known as "dead Zn", will eventually form on Co_3Ni_1-MOF, which is consistent with the e*x situ* SEM results (Fig. S17c). The presence of "dead Zn" can occupy the active sites and cause damage to the structure of the material until collapse, seriously affecting the electrochemical performance of the electrode material.[21] The modified BS-MOF-10 shows higher reversibility of Zn^{2+}, which can buffer the structural changes during the electrochemical process, thus exhibiting excellent electrochemical stability. Meanwhile, the S element is also uniformly distributed in BS-MOF-10 after cycling (Fig. S17h), indicating the stability of the BS-MOF-10 structure.

4 References

1 D. Chen, M. Lu, B. Wang, R. Chai, L. Li, D. Cai, H. Yang, B. Liu, Y. Zhang and W. Han, *Energy Storage Mater.*, 2021, **35**, 679-686.

2 N. Zhang, M. Jia, Y. Dong, Y. Wang, J. Xu, Y. Liu, L. Jiao and F. Cheng, *Adv. Funct. Mater.*, 2019, **29**, 1807331.

3 W. Yu, R. Ding, Z. Jia, Y. Li, A. Wang, M. Liu, F. Yang, X. Sun and E. Liu, *Adv. Funct. Mater.*, 2022, **32**, 2112469.

4 Y. Zhou, X. Tong, N. Pang, Y. Deng, C. Yan, D. Wu, S. Xu, D. Xiong, L. Wang and P. K. Chu, *ACS Appl. Mater. Interfaces*, 2021, **13**, 34292-34300.

5 Y. Chen, D. Ni, X. Yang, C. Liu, J. Yin and K. Cai, *Electrochim. Acta*, 2018, **278**, 114-123.

6 S. Maiti, A. Pramanik, U. Manju and S. Mahanty, *ACS Appl. Mater. Interfaces*, 2015, **7**, 16357-16363.

7 J. Sunil, C. Narayana, G. Kumari and K. Jayaramulu, *Chem. Soc. Rev.*, 2023, **52**, 3397-3437.

8 P. W. Sayyad, N. N. Ingle, G. A. Bodkhe, M. A. Deshmukh, H. K. Patil, S. M. Shirsat, F. Singh and M. D. Shirsat, *Radiat Eff. Defects Solids*, 2021, **176**, 274-283.

9 A. Mesbah, P. Rabu, R. Sibille, S. Lebègue, T. Mazet, B. Malaman and M. François, *Inorg. Chem.*, 2014, **53**, 872-881.

10 J. Yang, C. Zheng, P. Xiong, Y. Li and M. Wei, *J. Mater. Chem. A*, 2014, **2**, 19005-19010.

11 K. Zhou, W. Li, R. Huang, J. Liang, J. Chen, Y. Bao, D. Han and L. Niu, *J. Colloid Interface Sci.*, 2024, **658**, 459-467.

12 Z. Peng, C. Yang, Q. Zhao, F. Liang, S. Yun, R. Liu, Z. Zhang, Y. Liao and H.-C. Chen, *J. Colloid Interface Sci.*, 2022, **607**, 61-67.

13 Z. Zhu, R. Zhang, J. Lin, K. Zhang, N. Li, C. Zhao, G. Chen and C. Zhao, *J. Power Sources*, 2019, **437**, 226941.

14 W. Shang, W. Yu, X. Xiao, Y. Ma, P. Tan and M. Ni, *J. Power Sources*, 2021, **483**, 229192.

15 L. Jiang, L. Li, S. Luo, Z. Zhang, Y. Wu and Y. Qing, *Ind. Crops Prod.*, 2023, **201**, 116924.

16 C. Xu, J. Liao, C. Yang, R. Wang, D. Wu, P. Zou, Z. Lin, B. Li, F. Kang and C.-P. Wong, *Nano Energy*, 2016, **30**, 900-908.

17 G. Li, Y. Tang, S. Cui, H. Chen, H. Chong, L. Han and H. Pang, *Adv. Funct. Mater.*, 2024, 2401586.

18 B. Jia, D. Zhu, S. Zhou, S. Luo, Z. Liu, B. Li and M. Liu, *Chem. Commun.*, 2023, **59**, 2950-2953.

19 D. Zhang, J. Zhang, J. Li, C. Li, Y. Li, Y. Liu and R. Zhang, *RSC Adv.*, 2022, **12**, 20447-20453.

20 L. Zhou, X. Zhang, D. Zheng, W. Xu, J. Liu and X. Lu, *J. Mater. Chem. A*, 2019, **7**, 10629-10635.

21 T. Wang, C. Li, X. Xie, B. Lu, Z. He, S. Liang and J. Zhou, *ACS Nano*, 2020, **14**, 16321-16347.